Physics in Medicine &
Biology

Achieving high-resolution spatial mapping of dose and linear energy transfer in ion-beam therapy

IOP Publishing Phys. Med. Biol. 70 (2025) 215008 https://doi.org/10.1088/1361-6560/ae128f

Physics in Medicine & Biology

IPEM Institute of Physics and Engineering in Medicine

PAPER

Achieving high-resolution spatial mapping of dose and linear energy transfer in ion-beam therapy

Mads Lykke Jensen[1,*], **Michele Togno**[2], **Iván D Muñoz**[3,4], **Stephan Brons**[5], **Oliver Jäkel**[4,5], **Eduardo G Yukihara**[1] and **Jeppe Brage Christensen**[1]

[1] Department of Radiation Safety and Security, Paul Scherrer Institute (PSI), Villigen, Switzerland
[2] Center for Proton Therapy, Paul Scherrer Institute (PSI), Villigen, Switzerland
[3] Department of Radiation Oncology, Heidelberg University Hospital (UKHD), Heidelberg, Germany
[4] Division of Medical Physics in Radiation Oncology, German Cancer Research Center (DKFZ), Heidelberg, Germany
[5] Heidelberg Ion-Beam Therapy Center (HIT), Department of Radiation Oncology, Heidelberg University Hospital (UKHD), Heidelberg, Germany
[*] Author to whom any correspondence should be addressed.

E-mail: mads.jensen@psi.ch

Keywords: 2D mapping, LET, OSL, dosimetry, radiotherapy, proton therapy, ion-beam therapy

Supplementary material for this article is available online

OPEN ACCESS

RECEIVED
13 May 2025

REVISED
2 October 2025

ACCEPTED FOR PUBLICATION
13 October 2025

PUBLISHED
24 October 2025

Abstract

Objective. We present a novel detector system capable of simultaneously obtaining two-dimensional (2D) dose and linear energy transfer (LET) maps from Al_2O_3 films of sizes up to (190×190) mm^2 using optically stimulated luminescence (OSL). *Approach.* The system is based on the OSL from doped Al_2O_3 films measured using pulsed stimulation and time-resolved OSL detection. The system was calibrated in ^{1}H-, ^{4}He-, and ^{12}C-ion beams. The minimal detectable dose (MDD), response homogeneity, pixel cross-stimulation, and precision were also investigated. To demonstrate the system's performance, 2D maps of dose and LET of a proton Bragg curve were measured. *Main results.* The system was demonstrated to be capable of obtaining absorbed dose and LET 2D maps with a spatial resolution set to (1.0×1.0) mm^2. The system was calibrated over a clinically relevant range of LET values and characterized through assessment of MDD (<25 mGy), readout protocols, response homogeneity, precision, and relative detector efficiency. Dose and LET were found to be measurable with precisions of 3.2% and 10%, respectively. *Significance.* To our knowledge, this is the first passive detector system capable of measuring LET and dose simultaneously in 2D with a 1.0 mm^2 spatial resolution requiring no prior information. Such properties are required to experimentally validate simulated dose and LET distributions in ion-beam therapy, paving the way for sub-mm mapping of radiation-induced relative biological effectiveness.

1. Introduction

The ultimate goal of radiotherapy is to inflict radiation-induced, irreversible biological damage to cancerous tissue while sparing surrounding healthy tissue to the greatest extent possible. Compared to conventional radiotherapy, this goal is more effectively achieved with ion-beam therapy, where charged particles such as protons and heavier ions deliver a highly conformal dose to the tumor by exploiting the particles' finite range and sharp dose rise, followed by a steep dose fall-off close to the end of their range, known as the Bragg peak.

The radiobiological effect in ion-beam therapy, quantified by the relative biological effectiveness (RBE), can be considerably higher than that of conventional photon therapy, due to the high ionization density around the particle's tracks. Although radiation-induced biological response can be measured experimentally (Sørensen *et al* 2011), non-biological quantities correlated to RBE are often used as

proxies in simulations and experiments, as these are considerably easier to simulate and measure experimentally in a reliable and repeatable manner.

Among other physical quantities, RBE varies with ionization density (Guan *et al* 2018, Paganetti *et al* 2019, Underwood and McMahon 2019, Karger *et al* 2021), quantifiable through radiation quality metrics (RQMs). Although the ideal mapping between RBE and a given RQM (Kalholm *et al* 2024, Parisi *et al* 2024), and the optimal choice of RQM for this mapping (Lühr *et al* 2017, Christensen *et al* 2023, Kalholm *et al* 2023), is still heavily debated, there are multiple models relating RBE to dose-averaged linear energy transfer (LET) (Scholz *et al* 2020).

LET is defined as the mean energy loss per unit path length along the ionizing particle track (ICRU-85 2011). Because the LET depends on the particle charge and energy, it is necessary to average the LET to obtain a representative value when assessing LET from a clinically relevant field. This is traditionally done using dose to weigh each contribution to the LET, which is referred to as the dose-averaged LET ($\overline{\mathrm{LET}}_{\mathrm{D}}$). The choice of weight and scoring approach is, however, not standardized, which makes clear reporting of the LET calculation method essential (Lühr *et al* 2017, Kalholm *et al* 2021, Hahn *et al* 2022).

$\overline{\mathrm{LET}}_{\mathrm{D}}$ may be used as a proxy to optimize the RBE-weighted dose (RBE $\times$ physical dose) in treatment planning. Consequently, the implementation of LET optimization in treatment planning systems (TPSs) is a topic of increasing interest (Traneus and Ödén 2019, Deng *et al* 2021, Janson *et al* 2024), with studies showing its potential to improve treatment outcomes (McIntyre *et al* 2023).

However, recent studies have found systematic toxicity patterns in patients who underwent proton therapy that do not correlate as expected with the voxel-evaluated $\overline{\mathrm{LET}}_{\mathrm{D}}$ values (Garbacz *et al* 2021, Niemierko *et al* 2021, Vestergaard *et al* 2025). This indicated discrepancy between simulations and/or RBE models and the actual biological response highlights the need for experimental systems capable of obtaining $\overline{\mathrm{LET}}_{\mathrm{D}}$ and dose maps over a clinically relevant area with a clinically relevant spatial resolution. Such a system would enable the experimental investigation of the RBE vs. $\overline{\mathrm{LET}}_{\mathrm{D}}$ relation, experimental investigation of appropriate RQM choices, and contribute to the development, verification, and quality assurance of $\overline{\mathrm{LET}}_{\mathrm{D}}$-optimized treatment plans (Mohan 2022, Kalholm *et al* 2024, Christensen *et al* 2024b).

The non-linear response observed in most existing detectors when exposed to high-LET radiation (Birks 1951, Khan *et al* 2010, Payne *et al* 2011, Nascimento *et al* 2022) makes their direct application for dose mapping challenging in ion-beam therapy. While such a detector under-response, often referred to as ionization quenching, has previously been used to assess LET by correlating relative detector efficiency to LET, this approach relies on an *a priori* information of the dose to assess the LET (Bilski 2006, An *et al* 2022).

Several systems capable of measuring LET without prior knowledge of dose have been developed (Christensen *et al* 2024b), each one with its own set of strengths and challenges. Active detector systems, including silicon-based detectors (Agosteo *et al* 2010, Poikela *et al* 2014, Samnø y *et al* 2020, Bachiller-Perea *et al* 2022, Félix-Bautista *et al* 2024) and tissue-equivalent proportional counters (TEPCs) (Conte *et al* 2020, Bianchi *et al* 2024), perturb the radiation field due to their geometric extent, making treatment plan investigations using, for example, anthropomorphic phantoms challenging. Silicon-based detectors enable two-dimensional (2D) lineal energy (which is the microdosimetric equivalent to LET) measurements with spatial resolution (Tran *et al* 2021, Guardiola *et al* 2023), which simultaneously limits the overall detection area to just a few square centimeters. Moreover, with sensitive volumes consisting primarily of silicon, correction factors are needed to convert the measured LET to LET in water or tissue. Conversely, TEPCs, which also measure lineal energy, are by design tissue-equivalent, but they are limited to low fluence rates and point measurements.

Passive systems capable of measuring LET are plentiful and have existed for decades (Somogyi *et al* 1976), but have previously been limited to either low fluences or point measurements. While solid-state nuclear track detectors are widely used in personal and space dosimetry to this day (Bolzonella *et al* 2022), their application is limited to small areas at fluences below those of clinical relevance. These detectors can resolve individual particle tracks, utilizing either material degradation under chemical etching, referred to as track etch detectors (TEDs) (Benton and Benton 2001), or radiophotoluminescence (RPL), referred to as fluorescent nuclear track detectors (Klimpki *et al* 2016, Muñoz *et al* 2024). At fluences where individual particle tracks start to spatially overlap, particle identification becomes challenging, which directly affects the quality of the obtained spectra. Moreover, as the readout protocols involve optical imaging and processing of individual tracks, detectors are usually quite small to reduce readout times.

Luminescence-based systems are noteworthy in this context, although they are typically limited to point measurements of LET. These include thermoluminescent (TL) detectors (Parisi *et al* 2020) and optically stimulated luminescence (OSL) detectors (Christensen *et al* 2024a), assessing LET similarly, with

the difference between these systems residing in the method of stimulating the luminescence. Spatially integrated RPL, as opposed to single-track-resolving, has also been demonstrated to offer information on LET through variations of its emission spectrum (Miyamoto *et al* 2014, Sholom and McKeever 2023).

Several studies have reported on the use of luminescence-based detector types for 2D mapping, but these are all limited to dose measurements with the possible expansion of correlating a well-characterized luminescence efficiency to LET. Again, this would rely on *a priori* knowledge of the dose to assess LET. Examples include scanning-laser readout systems (OSL and RPL detectors) (Ahmed *et al* 2016a, Saint-Hubert *et al* 2019, 2021) and imaging systems (TL and OSL detectors) (Gajewski *et al* 2016, Sadel *et al* 2023). Closely related to this contribution is the work by Ahmed *et al* (2016a, 2016b)utilizing a fast scanning laser for OSL stimulation of large Al_2O_3 films to retrieve high-resolution dose maps.

Al_2O_3 is well-known in dosimetry (Yukihara *et al* 2022), with capabilities of storing information on both absorbed dose and ionization density. The OSL spectrum of carbon-doped Al_2O_3 (Al_2O_3:C) is composed of two main components: a UV component centered at 335 nm with a lifetime of 1.64(3) ns (Bossin *et al* 2025), and a blue component centered at 415 nm with a lifetime of ∼35 ms (Yukihara and McKeever 2011). Emissions from these centers may be temporally separated through pulsed optical stimulation (Yukihara and McKeever 2006). The recombination centers responsible for the OSL bands are known to exhibit different ionization quenching behaviors when exposed to different radiation qualities (Yukihara *et al* 2015). Central to the technique employed in this work, the ratio of the UV and the blue emission intensities has been demonstrated to correlate well with different RQMs (Christensen *et al* 2023).

Whereas the spectrally integrated OSL signal from Al_2O_3:C is fairly stable over time, showing little to no signs of fading (Bøtter-Jensen *et al* 1997), changes in the intensity of the spectral components after irradiation have been observed (Christensen *et al* 2024a). This causes the UV/blue ratio to change over time after irradiation, which ultimately requires samples to be read out within a similar time slot post-irradiation as that of calibration samples. Interestingly, this phenomenon is much less pronounced for carbon- and magnesium-doped Al_2O_3 (Al_2O_3:C,Mg), with the UV/blue ratio appearing to stabilize after a few days, eliminating time-sensitive readout protocols and thus making this material favorable (Christensen *et al* 2024a).

In this contribution, we present a novel readout system capable of simultaneously retrieving 2D dose and $\overline{\mathrm{LET}}_\mathrm{D}$ maps with high spatial resolution from Al_2O_3 films of sizes up to $(190 \times 190)\,\mathrm{mm}^2$ using OSL. The system is based on pulsed stimulation of OSL that enables temporal decomposition of the spectral components comprising the Al_2O_3 OSL. We investigate the system's capabilities in terms of minimal detectable dose (MDD), response homogeneity, and spatial resolution. The system was calibrated using irradiations with protons, ^{4}He-, and ^{12}C-ions, and the performance of the system is demonstrated by mapping a Bragg curve of protons in 2D, providing both $\overline{\mathrm{LET}}_\mathrm{D}$ and corrected dose. To our knowledge, this is the first passive detector system capable of measuring $\overline{\mathrm{LET}}_\mathrm{D}$ and dose simultaneously in 2D without relying on *a priori* information.

2. Materials and methods

This study investigated the correlation of dose-averaged LET to the OSL response from OSL-active films based on two types of material, namely Al_2O_3:C and Al_2O_3:C,Mg (section 2.1) and appropriate models (section 2.2). A novel optical readout system was developed to extract 2D information from the films (section 2.3). Film preparation and readout followed a dedicated protocol (section 2.4), and irradiations were carried out using protons, ^{4}He-, and ^{12}C-ions at two separate facilities (section 2.5). To calibrate the system, $\overline{\mathrm{LET}}_\mathrm{D}$ values were determined through Monte Carlo simulations (section 2.6). System characteristics, including the MDD and the extent of pixel cross-stimulation, were also examined (section 2.7).

2.1. Al_2O_3 films

The prototype films used in this work were produced by Landauer Inc. and consist of a 47 μm thick layer of 15 μm median grain size Al_2O_3:C or Al_2O_3:C,Mg micro-powder on a 75 μm thick polyester substrate. For simplicity, we restrict the results to Al_2O_3:C,Mg only and refer to the supporting material for the corresponding Al_2O_3:C results. The films are flexible, can be cut to any shape, and are able to conform to non-complex surfaces with a negligible perturbation of the radiation field.

2.2. Detector response modeling

The relationship between the intensities of the blue emission band and the UV emission band of Al_2O_3 was described by a logistic function of the form

$$\mathcal{R}(m) = \frac{(\mathcal{R}_{\max} - \mathcal{R}_{\min})}{1 + \left(\frac{m}{m_0}\right)^{-k}} + \mathcal{R}_{\min} \ , \tag{1}$$

where $\mathcal{R}$ is the ratio between the temporally integrated, background-subtracted UV and blue signal, referred to as UV/blue ratio from this point on, $\mathcal{R}_{\max}$ and $\mathcal{R}_{\min}$ denote lower and upper asymptote values of the UV/blue ratio, respectively, m_0 is the inflection point, and k is the curve slope factor. Here, the choice of RQM for the independent variable, m, is left open, as the system may be calibrated to the preferred metric (Christensen *et al* 2023).

The relative detector efficiency, η, describing the extent of the ionization-induced quenching of the measured signal, may be expressed as

$$\eta = \frac{D_Q}{D_{Q_0}} \ , \tag{2}$$

where D_Q is the measured dose under a given radiation quality, and D_{Q_0} is the absorbed dose for a reference radiation quality. This was modeled as a logistic behavior like that described by equation (1), using the blue emission for dose assessment with $k < 0$. Although both emission bands could be used as a dose proxy, the blue emission was used for all dose assessments. The reason for this choice is twofold. First, the blue emission band reaches a stable signal level much faster than the UV band. Second, the higher intensity of the blue emission band yields a better signal-to-noise ratio. The direct relation between the relative detector efficiency and the UV/blue ratio was found to be described by a piecewise function of the form

$$\eta(\mathcal{R}) = \begin{cases} 1 & \text{if } \mathcal{R} < \mathcal{R}_0 \\ \exp\left[-\frac{1}{2}\left(\frac{\mathcal{R} - \mathcal{R}_0}{q}\right)^2\right] & \text{if } \mathcal{R} \geqslant \mathcal{R}_0 \end{cases} \ , \tag{3}$$

where $\mathcal{R}_0$ denotes the threshold ratio whereafter the relative detector efficiency decreases in a Gaussian manner with q denoting the width of the falloff.

2.3. Optical readout system

Figure 1 shows a drawing of the novel readout system developed to read the irradiated films in 2D. The system features a light-tight enclosure, enabling operation in ambient laboratory light conditions. Housed inside this enclosure is an XY-stage (ASR series, Zaber Technologies Inc. Vancouver, BC, Canada) handling the movement of the film over an area measuring $(205 \times 205)\,\text{mm}^2$ with a reported accuracy of 50 μm and a repeatability of $< 2\,\mu$m. To collect the emitted OSL photons, a photomultiplier tube (PMT) (H11870-02, Hamamatsu, Iwata City, Japan) is mounted above the stage, equipped with a 425 nm short pass filter (84–703, Edmund Optics, York, United Kingdom) and a Hoya U340 filter (46–439, Edmund Optics, York, United Kingdom) to filter out the stimulation light. The XY-stage is mounted on rods, making room underneath for the optical components responsible for the spatially confined stimulation of the film.

The stimulation light is provided by a green light-emitting diode (LED) with a wavelength centered at 505 nm (M505L4, Thorlabs GmbH, Bergkirchen, Germany), driven by an LED driver (LEDD1B, Thorlabs GmbH, Bergkirchen, Germany) featuring external triggering. The LED light is collimated using an aspheric condenser lens with a focal length of 20.1 mm (L_1) and filtered using a bandpass filter centered around 500 nm with a full width at half max of 40 nm (FBH500-40, Thorlabs GmbH, Bergkirchen, Germany), before passing through two orthogonally-oriented, adjustable slits. Using a 90:10 beam splitter, 90% of the light is directed towards the film, where the slit opening is imaged onto the film using an iris aperture and a plano-convex lens with a focal length of 25 mm (L_2). The remaining 10% of the LED emission is directed towards a photodiode (PD) (DET36A2, Thorlabs GmbH, Bergkirchen, Germany) to monitor the LED intensity and correct for any fluctuations.

The stage is equipped with a custom-built adapter, mounting a $(203 \times 203)\,\text{mm}^2$ large, transparent optical window (21–330, Edmund Optics, York, United Kingdom) on which the film is placed. This adapter truncates the effective stimulation area to $(190 \times 190)\,\text{mm}^2$. A 2.5 mm thick, $(203 \times 203)\,\text{mm}^2$ large colored glass filter (Filtertec V34, U.Q.G Limited, Cambridge, England) is placed on top of the

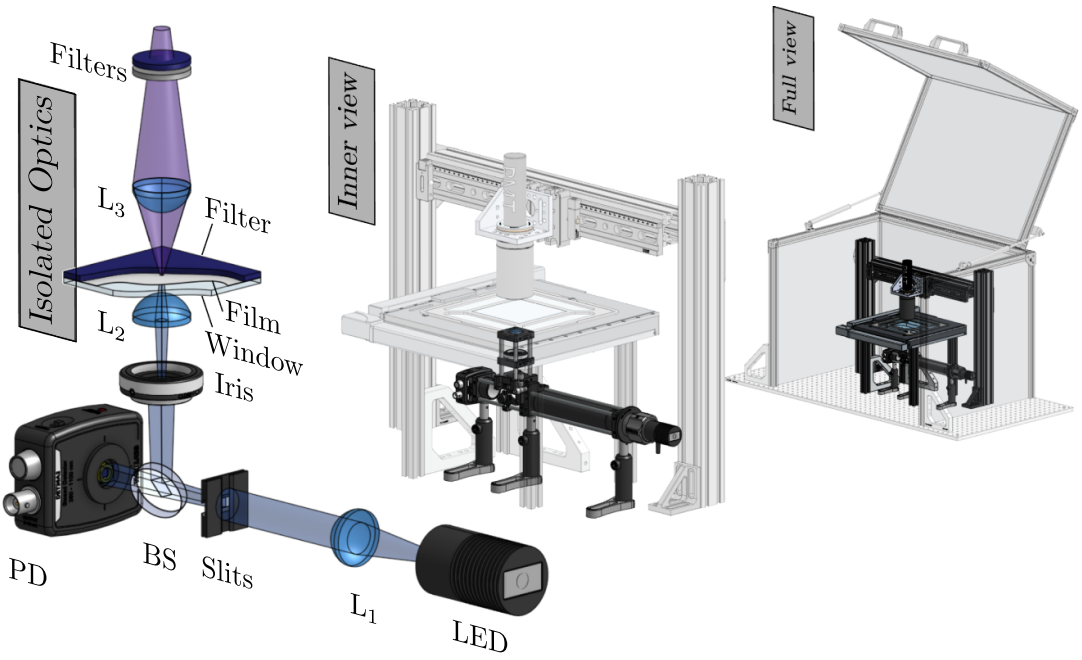

Figure 1. Drawing of the developed optical readout system showing a full view (background), a view of the inner components (middle), and an isolated view of the optical components (foreground). Some components are rendered transparent for illustrative purposes. The system includes a light-tight optical enclosure (visible in the full view) that enables operation under ambient light conditions. This enclosure houses the optical components, translation stages, and photomultiplier tube. The optical components responsible for film stimulation are highlighted in the foreground, comprising a light-emitting diode (LED), three lenses (L_i), two orthogonally oriented slits, a beam splitter (BS), a photodiode (PD), an iris aperture, and filters to isolate OSL from the stimulation light. The film is positioned between a transparent optical window and a colored glass filter, which, in addition to attenuation the stimulation light, serves to fixate the film and ensure it remains flat during readout. Note that the inter-component distances in the foreground drawing are not to scale.

sample, attenuating the stimulation light while simultaneously fixing the film in place during readout. At last, the emitted OSL is imaged onto the PMT through the attached filters by a double-convex lens with a focal length of 25 mm (L_3).

All data acquisition was handled by a data acquisition unit (DAQ; USB-6211, National Instruments, Austin, TX, USA) operating with a sampling rate of 100 thousand samples per second. The DAQ is configured to generate programmable waveforms, which are used as digital gating to trigger both PMT pulse counting and the LED. Moreover, the DAQ measures the analog voltage drop over a resistor connected to the PD. All hardware is operated by a custom-built, Python-based operating program.

2.4. Film preparation & readout protocols

All films were optically bleached using an LED flatbed with a peak wavelength of 530 nm (BT100100-530IC, Advanced Illumination, Rochester, Vermont, United States) for at least 24 hours before irradiation to reduce any signal from background irradiation. After bleaching, the films were loaded into light-tight bags consisting of 12 μm PET, 12 μm aluminum, and 75 μm low-density polyethylene to shield the films from ambient light. The films were irradiated inside these bags, yielding an effective sample thickness of 450 μm (2×125 μm being the films). A flow chart summarizing the described preparation along with the subsequent treatment steps, readout, and data analysis steps leading to the final dose and $\overline{\text{LET}}_\text{D}$ maps can be seen in figure 2.

To ensure identical irradiation conditions, each bag contained one film of each type, cut to the same dimensions. Both films were aligned with the exposed powder grain side facing the irradiation source, with the Al_2O_3:C,Mg film consistently placed on top of the Al_2O_3:C film.

To accommodate the different temporal behaviors of the intensity of emission from the two recombination centers, the films were read out within two to three weeks following irradiation. The readouts used a pulsed sequence with a frequency of 400 Hz (2.5 ms period), consisting of 1.00 ms of measuring with optical stimulation (measuring UV + blue emission), 0.48 ms of dwell time to allow for the LED to fully turn off, and 1.00 ms of measuring without stimulation (measuring blue emission only). The total number of such sequences per measurement, and the total number of measurements per pixel, varied between the measurements. In this work, measurement time refers to the total duration of a single pixel

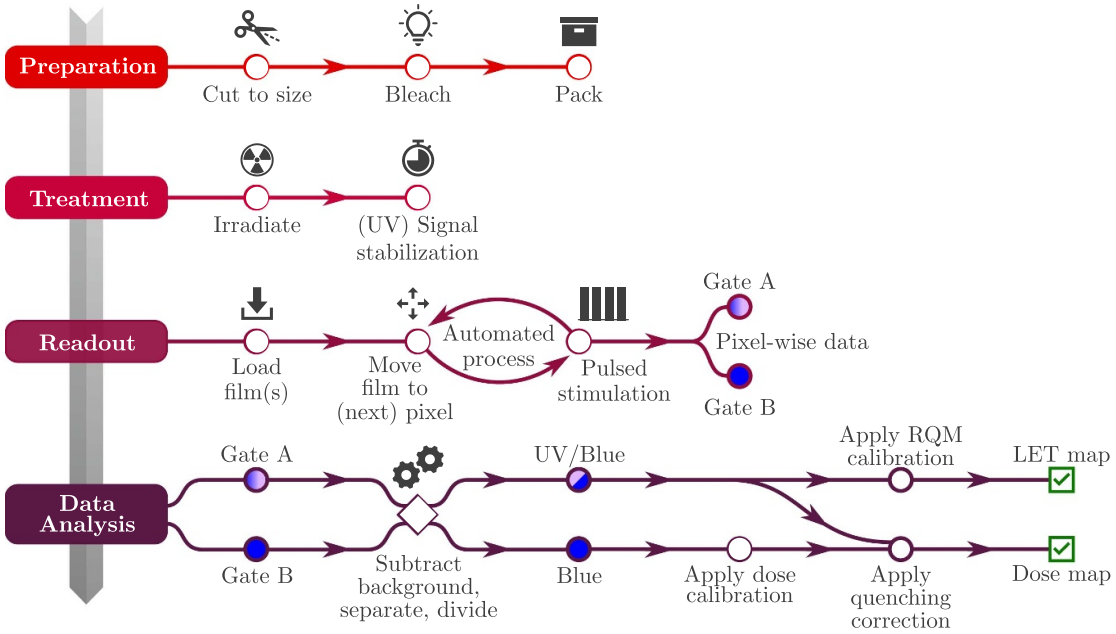

Figure 2. Flow chart of general steps needed to obtain dose and LET maps with the developed method, including all steps in preparation, treatment, readout, and data analysis.

measurement. The total duration of actual PMT measuring time in each channel is referred to as the integration time.

2.5. Irradiations

Irradiations were conducted at two separate facilities: the Center for Proton Therapy (CPT), Paul Scherrer Institute, Villigen, Switzerland, and the Heidelberg Ion-beam Therapy Center (HIT), Heidelberg University Hospital (UKHD), Heidelberg, Germany. Poly(methyl methacrylate) (PMMA) was used as a build-up material at CPT, whereas RW3 solid water was used at HIT. All doses measured with ionization chambers were ascribed an uncertainty of 1.6% ($k = 1$). All irradiations were conducted with doses below 1.2 Gy to ensure that the effect of overlapping ion tracks is negligible and the dose response is linear (Yukihara *et al* 2022). Table 1 provides an overview of all conducted irradiations.

For investigations of film homogeneity, pixel cross-stimulation, and assessment of the system calibration factor, films were irradiated with a homogeneous field of protons at CPT, with an integrated dose of 1.16(2) Gy measured using an Advanced Markus ionization chamber. The homogeneity of the field was assessed using a Lynx PT system (IBA Dosimetry GmbH, Germany), which showed that the field variation was less than 0.5% in the region of interest.

To establish a $\overline{\mathrm{LET}}_{\mathrm{D}}$ calibration of the detector system, several smaller films were irradiated at CPT and HIT, delivering homogeneous fields of varying $\overline{\mathrm{LET}}_{\mathrm{D}}$ values. The delivered doses were measured with Advanced Markus chambers for all irradiation configurations.

To test the dose and $\overline{\mathrm{LET}}_{\mathrm{D}}$ calibrations, a homogeneous field of protons was delivered to films through a PMMA wedge phantom to capture the entire Bragg curve.

2.6. Monte Carlo simulations

To establish a $\overline{\mathrm{LET}}_{\mathrm{D}}$ calibration of the system, the irradiation configurations were simulated using Monte-Carlo-based particle transport. Both dose and $\overline{\mathrm{LET}}_{\mathrm{D}}$ were scored to the detector positions. An overview of the simulations is provided in table 2. To estimate the uncertainty of a scored quantity to the detector position, the variation of the quantity following a 1-mm offset along the central beam axis in either direction was estimated. For the irradiations at HIT in the entrance region, this variation is negligible.

For a robust calculation of $\overline{\mathrm{LET}}_{\mathrm{D}}$, we adopted the scoring approach 'method C' as defined in Cortés-Giraldo and Carabe (2015). To comply with standard calculations of $\overline{\mathrm{LET}}_{\mathrm{D}}$ in proton therapy, which excludes contributions from particles heavier than protons, the scoring of radiation qualities excludes contributions from particles heavier than the primaries. For consistency, this approach was also applied to ^{4}He- and ^{12}C-ion beam simulations. Contributions from all particles were included in dose calculations.

Table 1. Summary of the conducted irradiations at the Center for Proton Therapy (CPT) at the Paul Scherrer Institute and Heidelberg Ion-Beam Therapy Center (HIT).

Particle	Facility	Energy (MeV u^{-1})	Field size (mm^2)	Al_2O_3 film size (mm^2)	Upstream material
^{1}H	CPT	227.2	120 × 200	85 × 95	24 mm PMMA
^{1}H	CPT	227.2	100 × 100	20 × 25	19 different amounts of PMMA in the interval 1.2–290 mm
^{1}H	CPT	129	35 × 90	85 × 95	PMMA wedge (93.2 mm wide, 150.3 mm high)[a]
^{1}H	HIT	99.74, 221.06	70 × 70	20 × 25	7.0 mm RW3
^{4}He	HIT	50.57, 65.94, 88.85, 220.51	70 × 70	20 × 25	7.0 mm RW3
^{12}C	HIT	173.63, 212.12, 292.42, 430.10	70 × 70	20 × 25	7.0 mm RW3

[a] To capture the entire field, the total dimensions of the film extended those of the delivered field.

Table 2. Monte Carlo simulation overview following the guidelines of Sechopoulos *et al* (2018).

Item	Description	Reference(s)
Code	`OpenTOPAS`, version 3.9.1	Perl *et al* (2012), Faddegon *et al* (2020)
Validation	Agreement between simulated and measured depth dose distributions.	Christensen *et al* (2022, 2023)
Timing	16 CPUs, CPU time 5×10^5 s	
Geometry	Detectors placed at the isocenter between PMMA (at CPT) or RW3 solid water slabs (at HIT). All quantities were scored in 1 mm^3 cubic voxels in a 2 cm × 2 cm area around the central beam axis.	
Physics list	A modular list consisting of `g4decay`, `g4h-elastic_HP`, `g4em-standard_opt4`, `g4h-phy_QGSP_BIC_HP`, `g4stopping`, `g4ion-binarycascade`.	
Scored quantities	Dose for all particles; $\overline{\mathrm{LET}}_\mathrm{D}$ to water, excluding contributions from secondaries heavier than the primary particle.	
Histories/uncertainties	10^8 primaries for each radiation quality, type A uncertainty negligible. Type B uncertainty assessed from the variation of the scored quantity in 1 mm.	

2.7. System characterization

To characterize the optical stimulation, the PMT and its light collection optics were temporarily replaced with a CCD camera and an objective to image the stimulation light spot at the sample plane. Moreover, the PD was used to temporally characterize the stimulation light source with the system operating under normal conditions, performing a pulsed readout with a measuring time of 1 second. This included logging of the gating signals for the PMT and LED, allowing for an assessment of the equipment synchronization.

2.7.1. Dose calibration

Following the TRS-398 (IAEA-TRS-398 2024), we determined the absorbed dose, D, from a system measurement, M, through the relation

$$\begin{aligned} D &= M \cdot N_{D_w,Q_0} \cdot \prod_i k_i \\ &= M \cdot N_{D_w,Q_0} \cdot k_{\mathrm{F}} \cdot k_{\mathrm{H}} \cdot k_\eta \ , \end{aligned} \tag{4}$$

where N_{D_w,Q_0} denotes the calibration factor for the system at reference conditions and k_i describes the correction factors for influence quantities.

For measurements with OSL-active films in this work, we limit the number of considered correction factors to a unity detector fading correction, $k_{\mathrm{F}} = 1$, with an uncertainty of 1%, a unity film inhomogeneity correction, $k_{\mathrm{H}} = 1.0$, with a non-zero uncertainty assessed experimentally, and the radiation-quality-dependent quenching correction factor, $k_\eta = 1/\eta$, determined through the relative detector efficiency (see equation (3)). The calibration factor, N_{D_w,Q_0}, was determined using the readouts from several of the films irradiated with protons in the entrance region, combined with the dose measurements from the Advanced Markus ionization chamber. We thus defined the entrance region protons with an energy of 227.2 MeV u^{-1} as our reference radiation quality.

2.7.2. Uncertainties

To report on the uncertainties of the derived dose and $\overline{\mathrm{LET}}_{\mathrm{D}}$, we follow the guidelines suggested by Lechner and Palmans (2025), listing each quantity's contribution to the uncertainty. This includes the type of the uncertainty contribution (statistical, A, or systematic, B), the underlying probability distribution function (PDF), the relative uncertainty of the quantity, u_i, and the final quantity's sensitivity towards the uncertainty of this parameter. The sensitivity coefficient, c_i, is determined as

$$c_i = \frac{\partial \mathcal{J}}{\partial p_i} \frac{p_i}{\mathcal{J}} \ , \tag{5}$$

where $\mathcal{J}(p_1, p_2, \ldots, p_n)$ denotes the expression for the parameters of interest, e.g. equation (4) and p_i denotes the ith parameter. The contribution uncertainty of the ith parameter to the total uncertainty is calculated as $\sqrt{(c_i \cdot u_i)^2}$. We assume no covariance between the parameters in all calculations.

2.7.3. MDD

As part of the system characterization, the MDD, the homogeneity of the film response, and the background levels were assessed through the readout of irradiated films before and after optical bleaching. The distribution of pixel values was used to assess the average signal and associated sample spread from all included pixels, and the MDD at reference conditions was determined following the ISO 11 929 standard (ISO-11929-1 2019), which is briefly summarized in the supplementary material. The MDD was calculated for different integration times to assess the system's performance as a function of readout time per pixel. Moreover, after characterization of the relative detector efficiency, i.e. the correction factor for radiation quality in equation (4), the MDD was determined as a function of the UV/blue ratio and the $\overline{\mathrm{LET}}_{\mathrm{D}}$.

2.7.4. Cross-stimulation of pixels

During the readout of a pixel, the measured signal is recorded as originating from the coordinates belonging to the center of this pixel. However, stimulation of neighboring pixels may occur during the readout of the primary pixel, which will thus be recorded under false origin. Consequently, the signal attributed to the primary pixel would be artificially higher, and when the neighboring pixels contributing to this effect are read out, the signal from these would be artificially lower. We refer to this effect as pixel cross-stimulation.

The extent of any cross-stimulation of pixels was assessed using a dedicated readout protocol of films irradiated with low-LET protons delivering a homogeneous dose profile. It was assumed that only nearest neighbors would contribute to a relevant extent to cross-stimulation, and we divided the total region exhibiting optical stimulation into five smaller regions; the primary region containing only the center pixel area, and four identical secondary regions, containing the part of the four neighboring pixels being stimulated during the readout of the center pixel. The dedicated protocol was divided into three groups of pixels: center pixels, neighboring pixels, and remaining pixels. Based on the readout from these groups of pixels, the fractional relation between central and neighboring pixels was determined as a

function of their respective integration times, t_C and t_N. This fraction, $\mathcal{F}(t_N, t_C)$, was fitted to a model of the form

$$\mathcal{F}(t_N, t_C) = \frac{\frac{\tau_p}{\tau_s}\left(1 - e^{-t_N/\tau_p}\right)\left(\tilde{A} + e^{-t_C/\tau_s} - 1\right) + \left(1 - e^{-t_N/\tau_s}\right)\left(3 + e^{-t_C/\tau_p}\right)}{\tilde{A}\frac{\tau_p}{\tau_s}\left(1 - e^{-t_C/\tau_p}\right) + 4\left(1 - e^{-t_C/\tau_s}\right)}, \tag{6}$$

where τ_p and τ_s are the lifetimes of the signal from the primary and secondary regions, respectively, and $\tilde{A}$ is the fractional area of the primary and secondary regions. We refer to the supporting material for a thorough explanation and derivation of the model.

3. Results

3.1. Pulsed stimulation characterization

The spatial and temporal characteristics of the light source used for stimulation of the OSL are shown in figure 3. The spatial extent of the stimulation region is displayed in figure 3(a) and was found to be $(1.0 \times 1.0)\,\mathrm{mm}^2$ with $\geqslant$90% intensity ensured within the central 950 μm in both dimensions. Using several profiles along each dimension, the intensity profile was found to fall below the chosen threshold value of 10 times the background level within just 40 μm at each edge of the region.

The temporal profile of the LED shown in figure 3(b) yielded a rise time of 135 μs (95% of maximum power) and a fall time of 155 μs (5% of maximum power), showing the choice of a 0.48 ms gating delay to be sufficient for temporal separation of the emission bands. The LED was found to be stable over time, with a variation of less than 1% over several hours, which was readily corrected for using the available PD signal.

3.2. Pixel cross-stimulation

The assessment of the extent of cross-stimulation is summarized in figure 4. The dedicated readout protocol to assess the extent of cross-stimulation of pixels is graphically summarized in figure 4(a). The readout protocol consisted of: center pixels, which were read out first with varying integration times, neighboring pixels, which were read out next with a fixed integration time of 50×0.4 s, and remaining pixels, which were read out last with an integration time of 10×0.8 s. The center-to-neighbor pixel fraction, $\mathcal{F}(t_N, t_C)$, was determined for each spot and used to fit the model (equation (6)), which is shown in figure 4(b) along with the fractions. The residuals between the model and the data are shown in figure 4(c), showing the model to describe the observed fractional relationship to a satisfactory extent.

The fit yielded the lifetimes $\tau_p = 2.454(7)$ s and $\tau_s = 257.5(6)$ s and a fractional area of $\tilde{A} = 3.537(5)$. In other words, the lifetimes, and thus the stimulation cross-section, of the signal from the primary and secondary regions were found to differ by two orders of magnitude. Moreover, the affected areas of the regions were found to differ by a factor of $\sim$3. Hence, we concluded that no corrections for pixel cross-stimulation readout were needed.

3.3. Detector response

Figure 5(a) shows the background-subtracted and temporally integrated readout from an Al_2O_3:C,Mg film after irradiation with a homogeneous field of proton pencil beams delivering an integrated dose to water of 1.16(2) Gy. The displayed data is limited to the central $(75 \times 85)\,\mathrm{mm}^2$ region of the $(85 \times 95)\,\mathrm{mm}^2$ film, and the color bar indicates the pixel counts measured in the blue emission band. The observed gradient across this readout indicates a systematic error.

The histograms in figure 5(b) shows the measurement distributions of readout after irradiation (blue) and after bleaching (orange), where relevant statistical quantities are annotated in the panel. The measured spread of the signal retrieved from the included pixels in panel a) as a function of integration time is shown in figure 5(c), along with derived statistical and systematic spreads. These results indicate a systematic error of 2.5%, which may largely be attributed to the inhomogeneous film response observed in figure 5(a)

The MDD at reference conditions is plotted as a function of integration time in figure 5(d). The major contributor to the observed linear behavior resides in the dark current of the PMT, scaling linearly with integration time.

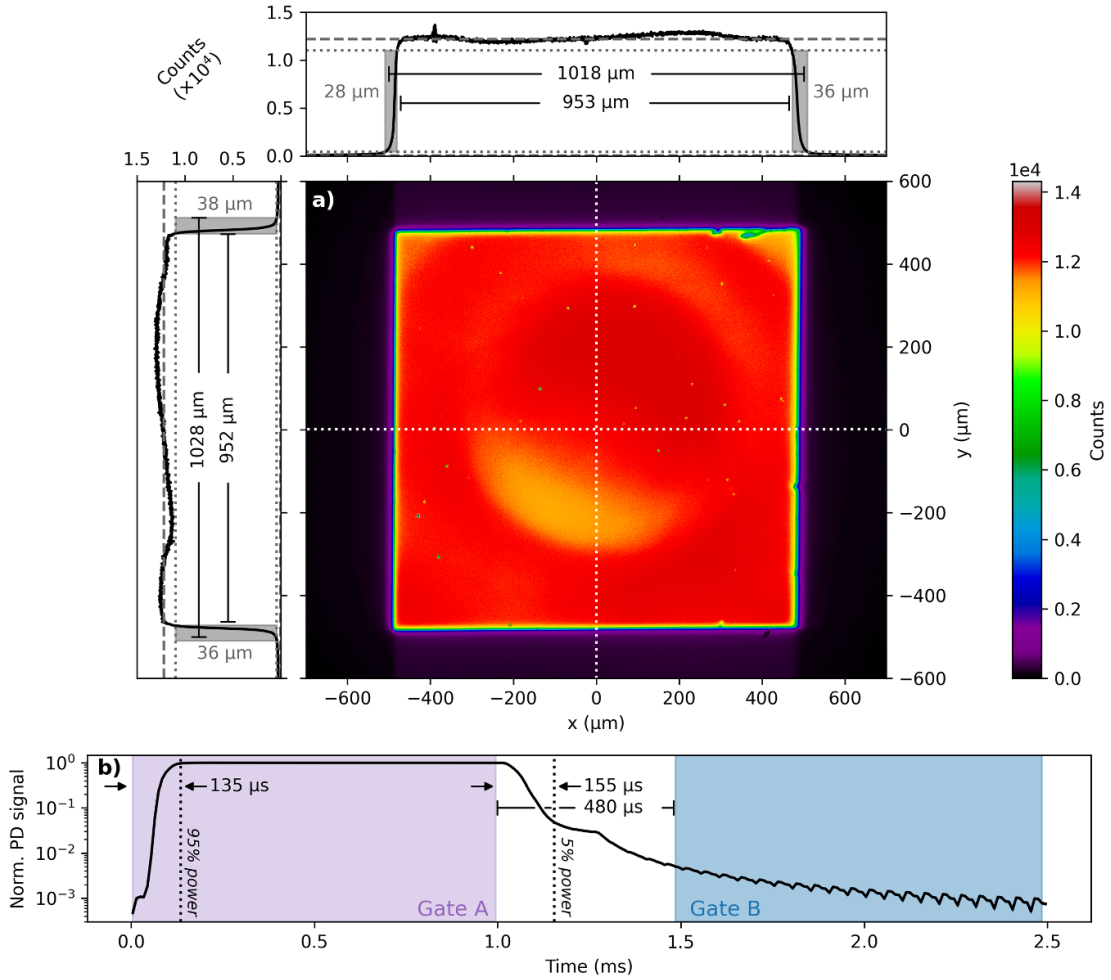

Figure 3. Spatial and temporal characterization of the light source used for stimulation of OSL. (a) Intensity profile of the stimulating spot in the sample plane, acquired with a CCD camera and imaging optics. The dashed lines on the image indicate the locations of the plotted intensity cross-sections shown above and beside the image. The plots include hatched areas representing the average gradient width of the intensity profile, defined using thresholds of 10 times the background and 90% of the spot's median intensity. These thresholds are marked with dotted lines on the plots, while dashed lines indicate the background and median values. Relevant distances are noted directly on the plots. (b) Temporal profile of the LED used for stimulation, measured with a photodiode, along with the gating signals used for OSL measurements. The LED exhibited a rise time of 135 μs (95% of maximum power) and a fall time of 155 μs (5% of maximum power). The profiles represent the average of 400 consecutive sequences (2.5 ms period) sampled at 100 kHz.

3.4. $\overline{\text{LET}}_{\text{D}}$ calibration

The simulated dose and $\overline{\text{LET}}_{\text{D}}$ profiles as a function of depth in PMMA for the 227.2 MeV u^{-1} proton irradiations are shown in figure 6. The insets display the readout of the Al_2O_3:C,Mg films at seven selected depths, with both dose and $\overline{\text{LET}}_{\text{D}}$ proxies shown in the form of blue and UV/blue ratios, respectively. The displayed data is background-subtracted, temporally integrated, and limited to the central (10×15) mm^2 region of the (20×25) mm^2 films.

Using the retrieved distributions from the irradiated films, the proxies were calibrated against the simulated dose and $\overline{\text{LET}}_{\text{D}}$ at the depth of each sample as shown in figure 7. The $\mathcal{R}$ = UV/blue ratio and the relative detector efficiency η are plotted against $\overline{\text{LET}}_{\text{D}}$ in panels figures 7(a) and (b), respectively. Vertical error bars indicate the spreads on the retrieved data, and the horizontal error bars are propagated from the simulations. Both $\mathcal{R}$ and η were fitted with a logistic fit (equation (1)), which is plotted in red with the resulting fit parameters denoted in each panel. The residuals between the fit and data are displayed at the bottom of each panel.

Figure 8(a) shows the same data as in figure 7(b), but with the relative detector efficiency plotted as a function of the UV/blue ratio instead of $\overline{\text{LET}}_{\text{D}}$. The model described by equation (3) was fitted to the data and is plotted as a red line. The fitting parameters are denoted on the panel, and residuals between the fit and the dataset are plotted at the bottom of the panel. Panels figures 8(b) and (c) show the MDD as a function of $\overline{\text{LET}}_{\text{D}}$ and $\mathcal{R}$, respectively, calculated using the detector calibration factor and the fitted relative detector efficiencies.

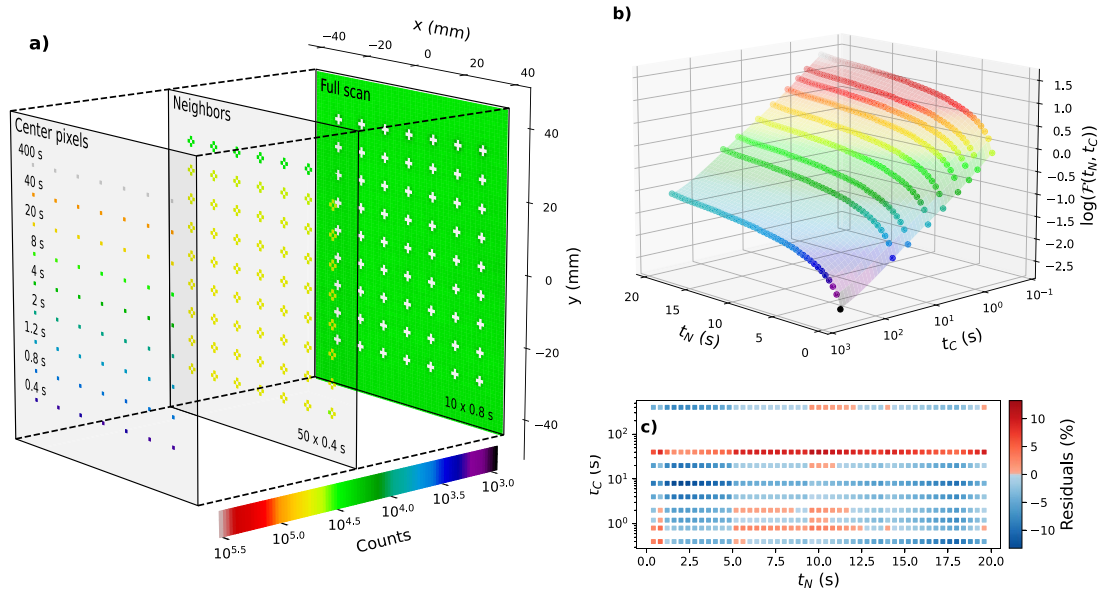

Figure 4. Readout of Al_2O_3:C,Mg film after homogenous irradiation using a protocol to assess the extent of pixel cross-stimulation. The Al_2O_3:C,Mg film, measuring (85×95) mm^2, was irradiated with a homogenous field of protons delivering an integrated dose to water of 1.16(2) Gy. The data was retrieved in three different groups, as displayed in a layered presentation in panel (a). *The center pixels* were read out row-by-row with varying integration times, indicated next to each row. *The neighboring pixels* were stimulated sequentially with an integration time of 0.4 s per pixel, repeated 50 times (totaling 50×0.4 s per pixel). *The remaining pixels* were read out with an integration time of 0.8 s per pixel, repeated 10 times (totaling 10×0.8 s per pixel). All displayed data is temporally integrated and background subtracted. The logarithmic color bar indicates pixel counts and is consistent across all data groups in this panel. (b) The center-to-neighbor pixel fraction, $\mathcal{F}(t_N, t_C)$, with t_N and t_C being the neighbor and center integration times, respectively, was fitted with the model described by equation (6). All fractions were calculated as the weighted arithmetic mean of pixel groups with identical center pixel integration times. The fit yielded the lifetimes $\tau_p = 2.454(7)$ s and $\tau_s = 257.5(6)$ s and a fractional area of $\tilde{A} = 3.537(5)$. Panel (c) displays the residuals between the model and the data, plotted using a discontinuous color scale, where negative residuals are shown in blue and positive residuals in red.

3.5. Uncertainty budgets

The uncertainty budgets of the dose and $\overline{\text{LET}}_\text{D}$ are presented in tables 3 and 4, respectively. We report the uncertainty budgets for the entrance region of irradiation with protons of mean energy 227.2 MeV u^{-1}, at a water equivalent thickness (WET) of 20 mm with a total dose of 1.82 Gy, as recommended for ionization chambers by TRS-398 (IAEA-TRS-398 2024). As the sensitivity and relative uncertainty implicitly depend on the film response, and thus the dose and $\overline{\text{LET}}_\text{D}$, we furthermore report the uncertainty budgets in the Bragg peak region at a WET of 330 mm for the same dose.

Contributions from the fitting parameters in the quenching correction factor (k_η, see equation (3)) are listed separately to eliminate covariance considerations. Moreover, the RQM calibration in table 4 is derived from the fundamental positioning uncertainty of samples during the calibration measurements (1.0 mm) as opposed to the fitting uncertainty of the empirically chosen equation (1).

Equivalent budgets for Al_2O_3:C can be found in the supplementary material.

3.6. Bragg curve

The readout from the Al_2O_3:C,Mg film after irradiation with the PMMA wedge is shown in figures 9(a) and (b), displaying the ionization quenching corrected dose and $\overline{\text{LET}}_\text{D}$ maps, respectively. The displayed data was background-subtracted and temporally integrated before it was scaled and/or corrected with the fitted models from figures 7(a) and 8(a). Figure 9(c) shows the average profiles along the central 10 mm wide strip marked by the white dashed lines in panels (a) and (b). For reference, the uncorrected dose profile is also plotted.

4. Discussion

We have presented, characterized, and demonstrated the performance of a custom-built detector system with high spatial resolution capable of simultaneously measuring dose and $\overline{\text{LET}}_\text{D}$. The system relies on thin Al_2O_3 films as the active detector material and a spatially well-confined, pulsed stimulation for readout of the stored information.

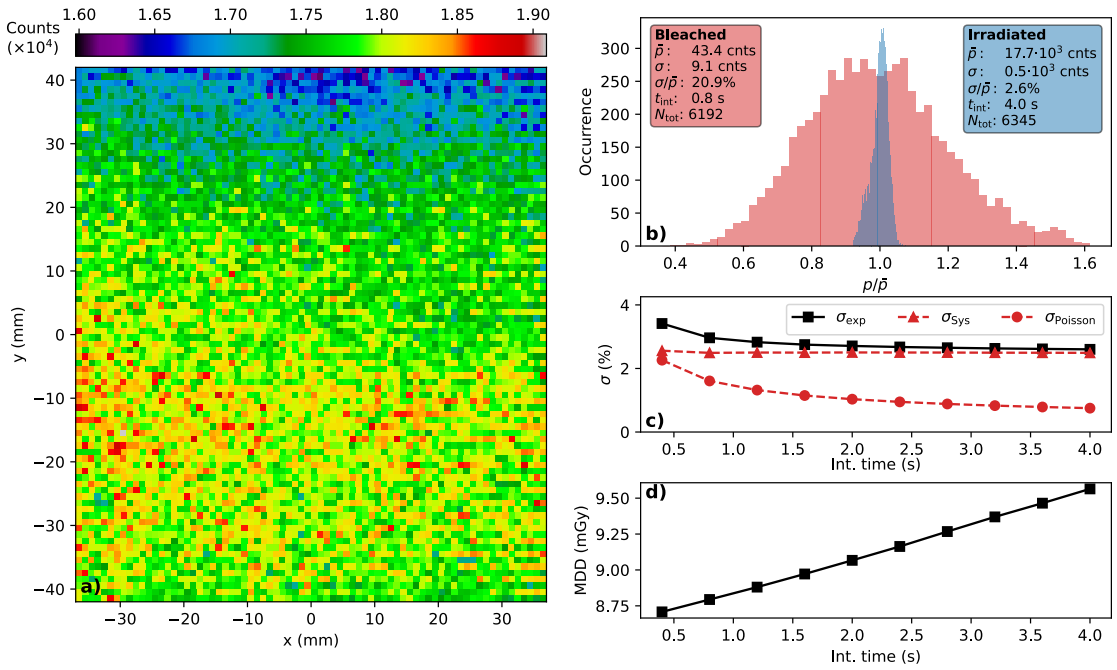

Figure 5. Assessment of the homogeneity of the readout from the Al_2O_3:C,Mg film after irradiation with a homogeneous field of proton pencil beams delivering an integrated dose-to-water of 1.16(2) Gy. (a) Background-subtracted and temporally integrated signal of the blue emission (gate (B) from the central (75×85) mm^2 of a (85×95) mm^2 film. (b) Histograms of the retrieved signal after irradiation (blue) and after bleaching (orange). Relevant statistical quantities including the mean pixel values ($\bar{p}$), spreads (σ), integration times (t_{int}), and total number of pixels (N_{tot}) are annotated in the panel. (c) Measured spread (σ_{exp}) of the signal retrieved from the included pixels in panel (a) as a function of integration time, along with derived statistical ($\sigma_{Poisson}$) and systematic (σ_{sys}) spreads. (d) Minimal detectable dose (MDD) for reference conditions plotted as a function of integration time.

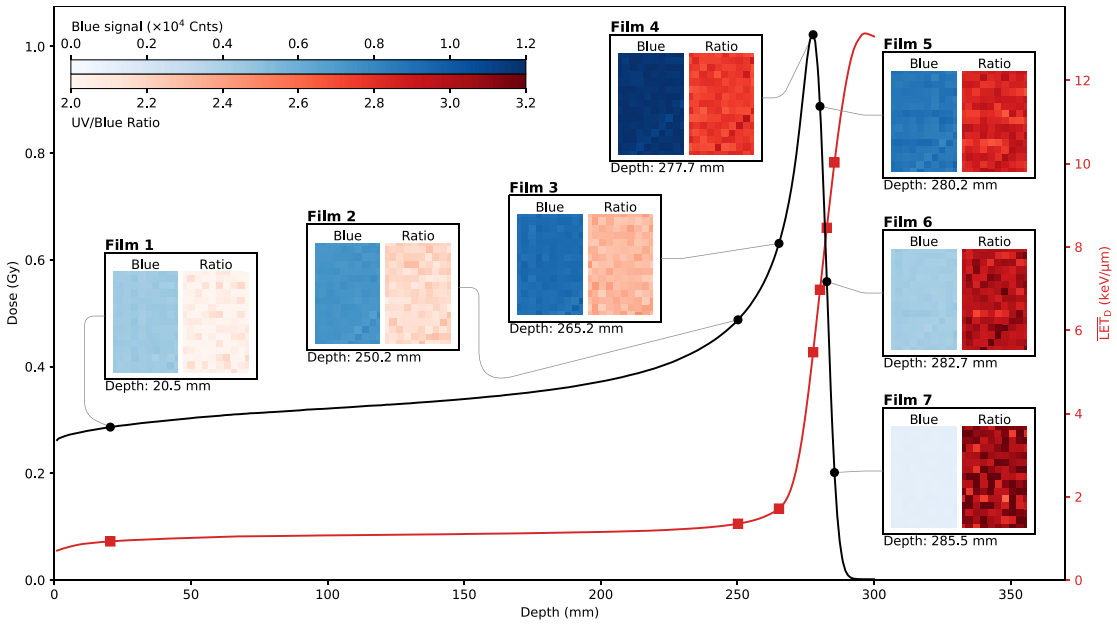

Figure 6. Selected readouts of the proton irradiation data series used for calibration of the system. The main figure displays the simulated dose (black) and $\overline{LET}_D$ (red) profiles as a function of depth in PMMA. The insets display the readout of the Al_2O_3:C,Mg films at seven selected depths, with both dose and $\overline{LET}_D$ proxies shown in the form of blue and UV/blue ratios, respectively. The displayed data is background-subtracted, temporally integrated (10 s measurement, 4.0 s integration), and limited to the central (10×15) mm^2 region of the (20×25) mm^2 films. The dose and $\overline{LET}_D$ consistently follow the blue and red color bars in the top left of the main figure across all insets. The depth of the films is indicated under each inset and marked on the profiles with black circles and red squares for dose and $\overline{LET}_D$, respectively.

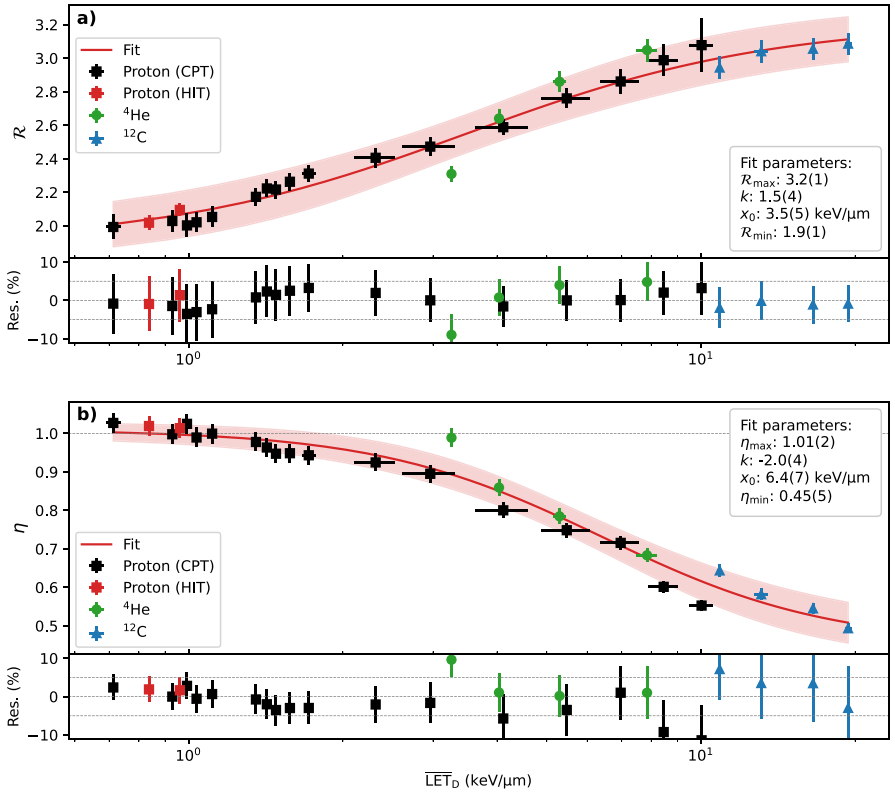

Figure 7. Calibration of the dose and LET proxies using a series of (20×25) mm^2 Al_2O_3:C,Mg films irradiated with different fields of varying $\overline{\text{LET}}_D$ values with different particle types. Panels (a) and (b) show the UV/blue ratio ($\mathcal{R}$) and the relative detector efficiency (η), respectively, plotted as a function of dose-averaged LET ($\overline{\text{LET}}_D$). The displayed data is background-subtracted, temporally integrated (10 s measurement, 4.0 s integration). Each data point represents the average of all pixels within the central (10×15) mm^2 of a sample, with the vertical error bars indicating the corresponding spreads ($k = 1$). The horizontal error bars are propagated from the simulations ($k = 1$). Both data sets have been fitted with a logistic function (equation (1)), which is plotted as red lines along with the corresponding confidence bands ($k = 1$). The fitting parameters are denoted on each panel, and residuals between the fits and data sets are plotted at the bottom of each panel.

Readout characteristics. As shown in figure 3(a), the system has a spatial resolution of (1.0×1.0) mm^2, dictated by the spatially well-confined stimulation light spot. The intensity profile of the spot was largely homogeneous across its area, highlighting the uniformity and spatial confinement of the stimulation. A faint circular structural feature is also visible in the spot image, presumably originating from direct imaging of the LED's internal structure.

The spatial resolution of the system can be changed to accommodate both smaller and larger pixel sizes through adjustments of the spot-defining slits (see figure 1). Such a change would, however, directly affect the system readout times, and increasing the spatial resolution will compromise the precision of the system reported in this work. Currently, the system is capable of reading out a (85×95) mm^2 film with a pixel measurement time of 1 s in less than three hours.

The system relies on the temporal decomposition of the OSL signal from the Al_2O_3 films, which is achieved through a fully adjustable pulsed readout protocol. The time-resolved measurement in figure 3(b), showing the pulsing sequence used in the presented work, demonstrates that a 0.48 ms gating delay is sufficient to ensure that the LED is fully turned off before the readout of the blue emission. Accounting for the observed rise and fall times of the LED could potentially improve the system capabilities, and the effects of changing the pulse profile are subject to further studies.

Negligible cross-stimulation of pixels. Given the microparticle form of the OSL-active material, scattering of the stimulating light is expected, which could prematurely stimulate sample regions during the readout. We assessed the extent of this effect using a dedicated readout protocol and a model to describe the observed data. Although the model is based on several assumptions, it was found to describe the observed data well, as shown in figure 4. Based on the fitted parameters, the lifetimes of the signal from the primary and secondary regions were found to differ by two orders of magnitude, and the affected

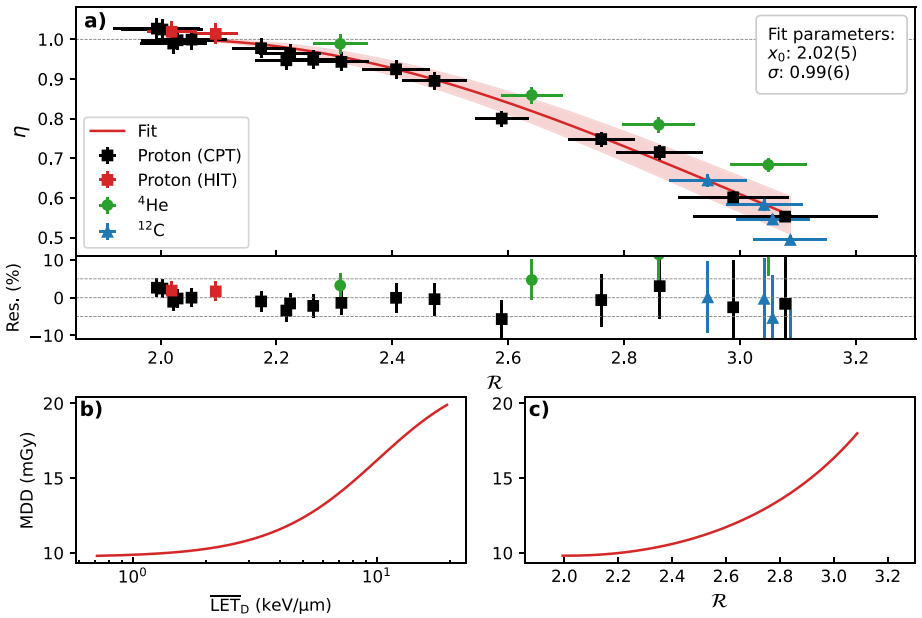

Figure 8. Internal detector calibration and assessment of minimal detectable dose. Panel (a) displays the same data as in figure 7(a), but with the relative detector efficiency plotted as a function of the UV/blue ratio ($\mathcal{R}$) instead of $\overline{\text{LET}}_\text{D}$. The data is fitted with the model described by equation (3), which is plotted as a red line along with the corresponding confidence band ($k = 1$). The fitting parameters are denoted on the panel, and residuals between the fit and the dataset are plotted at the bottom of the panel. Panels (b) and (c) show the MDD as a function of $\overline{\text{LET}}_\text{D}$ and $\mathcal{R}$, respectively, calculated using the detector calibration factor and the fitted relative detector efficiencies.

Table 3. Uncertainty budget of dose measurements with Al_2O_3:C,Mg films using 227.2 MeV u^{-1} protons with a delivered dose of 1.82 Gy at WETs of 20 mm (entrance) and 330 mm (peak).

			Sensitivity		Relative uncertainty (%)		Contributing uncertainty (%)	
Quantity	Uncertainty Type	PDF	Entrance	Peak	Entrance	Peak	Entrance	Peak
UV+Blue reading, M_Both	A	Poisson	0.0	2.7	0.34	0.35	0.0	0.95
Blue reading, M_Blue	A	Poisson	1.0	−1.7	0.59	0.68	0.59	1.2
Dose calibration, N_{D_w,Q_0}	B	Normal	1.0		1.6		1.6	
Fading correction, k_F	B	Normal	1.0		1.0		1.0	
Inhomogeneity correction, k_H	B	Normal	1.0		2.5		2.5	
Quenching correction, k_η								
↳ Threshold ratio, $\mathcal{R}_0$	B	Normal	0.0	−1.5	2.3		0.0	3.4
↳ Falloff width, q	B	Normal	0.0	−0.52	6.0		0.0	3.1
Total dose uncertainty							3.2	5.8

Table 4. Uncertainty budget of $\overline{\text{LET}}_\text{D}$ measurements with Al_2O_3:C,Mg films using 227.2 MeV u^{-1} protons with a delivered dose of 1.82 Gy at WETs of 20 mm (entrance) and 330 mm (peak).

			Sensitivity		Relative uncertainty (%)		Contributing uncertainty (%)	
Quantity	Uncertainty Type	PDF	Entrance	Peak	Entrance	Peak	Entrance	Peak
UV+Blue reading, M_Both	A	Poisson	15	8.3	0.34	0.35	5.0	2.9
Blue reading, M_Blue	A	Poisson	-15	-8.3	0.59	0.68	8.8	5.6
$\overline{\text{LET}}_\text{D}$ calibration	B	Normal	1.0		0.065	1.1	0.065	1.1
Total $\overline{\text{LET}}_\text{D}$ uncertainty							10	6.4

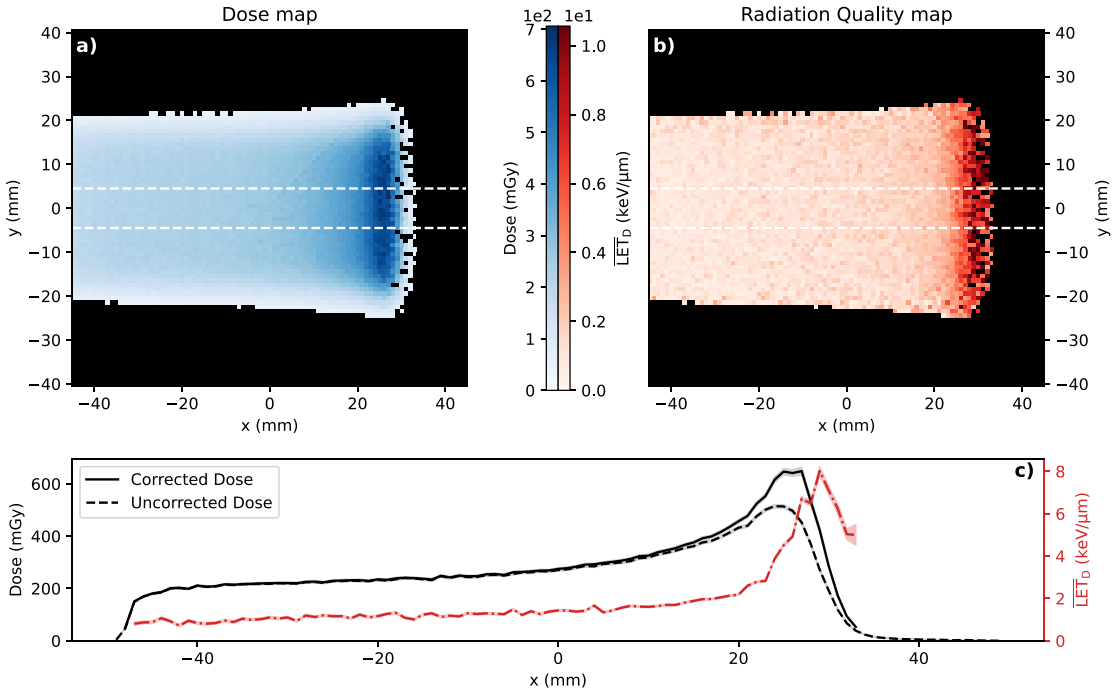

Figure 9. $\overline{\mathrm{LET}}_\mathrm{D}$ and corrected dose maps of a Bragg curve delivered to a (85×95) mm^2 Al_2O_3:C,Mg film using a wedge-shaped PMMA phantom and a series of proton pencil beams. The displayed data is background-subtracted, temporally integrated (6.0 s measurement, 2.4 s integration), and limited to the central (82×92) mm^2 region of the film. (a) Corrected dose map obtained by scaling the dose proxy with the dose calibration factor and correcting for the relative detector efficiency using the relative detector efficiency calibration (figure 8(a)) derived from the UV/blue ratio. (b) $\overline{\mathrm{LET}}_\mathrm{D}$ map obtained by applying the calibration derived from the calibration (see figure 7(a)) to the UV/blue ratio. Values falling outside the calibration range of the used calibrations or yielding a dose less than 50 mGy are displayed as black. (c) Profiles of the average dose and $\overline{\mathrm{LET}}_\mathrm{D}$ along the central 10 mm wide strip marked by the white dashed lines in panels (a) and (b). The corrected dose and $\overline{\mathrm{LET}}_\mathrm{D}$ profile are shown in black and red, respectively. Moreover, the uncorrected dose profile in the same region is shown as a dashed black line.

areas of the regions were found to differ by a factor of three. We thus conclude the effect of pixel cross-stimulation in the system to be negligible, requiring no need for corrections. This is consistent with the observation that only neighboring pixels to primary pixels with 400 s integration times in figure 4(a) shows drastically affected signal values.

Film uniformity. While the readout protocol of the system might be of negligible influence on the retrieved information, several other factors are of importance. As observed in the readout of the homogeneously irradiated film in figure 5(a), the film response is not uniform across the entire film, showing a gradient from the upper right corner to the lower left corner. We interpret this to be a result of an uneven distribution of the OSL-active powder on the films, which is consistent with the observation of a different gradient between films (see Al_2O_3:C readout in the supplementary material). The resulting distribution of the pixel values shown in figure 5(b) is widened by this inhomogeneity of the film, yielding a spread of 2.6%.

Using counting statistics to determine the statistical contribution to the observed spread, we found the systematic spread to be 2.5% and independent of the integration time, as expected. As the dose is calculated by scaling the measured signal from the blue emission, its precision is fundamentally limited by the systematic error attributed to film inhomogeneity. This limitation does not apply to the dose-averaged LET, which is derived from the UV/blue emission ratio. Any pixel-wise variation in the concentration of OSL-active particles would scale the intensity of both emission components identically, rendering this ratio independent of film inhomogeneities. Hence, the precision of the $\overline{\mathrm{LET}}_\mathrm{D}$ measurements is limited primarily by shot noise and calibration uncertainties.

The contribution from this systematic error to the dose uncertainty could be drastically reduced by applying a film-specific correction factor. Given the reusability of the films, such a correction map could easily be obtained prior to any irradiation and applied to the readout. This would only be advisable for measurements requiring high relative precision in dose, as the $\overline{\mathrm{LET}}_\mathrm{D}$ determination is stable towards film inhomogeneities.

MDD. We report MMDs of less than 10 mGy at reference conditions, where the main limitation originates from the contribution of dark current in the PMT, giving rise to the observed linear behavior with integration time in figure 5(d). When correction factors for the relative detector efficiency are applied, the MDD will be dominated by the uncertainties of the fitted model at high $\overline{\mathrm{LET}}_{\mathrm{D}}$ values, as shown in figure 8(b) and c, but even here the MDD is below 25 mGy.

Uncertainties. From the uncertainty budgets presented in tables 3 and 4, the precision in dose was found to be 3.2% in this entrance region and 5.8% in this Bragg peak region. This reduction in precision is ultimately caused by an increase in ionization quenching. As a result, a larger quenching correction is needed for compensation, and this correction is itself associated with a larger uncertainty. Moreover, the sensitivity of the raw readings also increases, which further contributes to the dose uncertainty.

The opposite behavior is observed in the $\overline{\mathrm{LET}}_{\mathrm{D}}$ precision, which improves from 10% in the entrance region to 6.4% in the Bragg-peak region. Owing to the shape of the diverging calibration curve, uncertainties in the UV/blue ratio near the logistic asymptotes lead to a higher sensitivity of the raw readings in the entrance region. This effect dominates the contribution from the calibration uncertainty.

Importantly, we note that the uncertainty in the UV/blue ratio propagates with higher sensitivity in the $\overline{\mathrm{LET}}_{\mathrm{D}}$ calculation than in the dose calculation due to the different models used for $\overline{\mathrm{LET}}_{\mathrm{D}}$ calibration (equation (1)) and detector efficiency characterization (equation (3)).

Al_2O_3:C results. The results for the Al_2O_3:C film presented in the supplementary material are arguably of better quality than those of Al_2O_3:C,Mg, which is largely related to the higher OSL intensity and consequently better signal-to-noise ratio of this film type. The Al_2O_3:C film was found to have MDDs below 15 mGy with very low correction factors across the range of the Bragg curve. Moreover, the systematic spread was found to be 1.5% for Al_2O_3:C, but this may reflect a coincidentally chosen more homogeneous piece of film. No need for corrections for pixel cross-stimulation was found for this film type. The uncertainty budgets for the entrance region yielded relative uncertainties of 2.4% and 9.2% for dose and $\overline{\mathrm{LET}}_{\mathrm{D}}$, respectively. In the Bragg peak region, these relative uncertainties were 3.8% and 3.5%. Al_2O_3:C should thus be considered for high-precision studies, where the downside of the necessary time schedules for readout is outweighed by the improved precision.

$\overline{\mathrm{LET}}_{\mathrm{D}}$ calibration. In this contribution, we calibrated the response from doped Al_2O_3 films against $\overline{\mathrm{LET}}_{\mathrm{D}}$ after irradiation with three different ion species, namely protons, ^{4}He- and ^{12}C-ions. Whereas the ^{4}He- and ^{12}C-ion data were acquired at quasi-monoenergetic conditions at the entrance regions to minimize measurement uncertainties, much of the proton data were acquired at the Bragg peak region and the distal edge of the Bragg curve. As a result, the high-LET proton measurements are associated with larger uncertainties, and the heavier ion data were used to supplement this region of the $\overline{\mathrm{LET}}_{\mathrm{D}}$ range for a better calibration in the clinically relevant range for proton treatments.

While the calibrations presented in figure 7 are applicable, it may be argued that data from the different ion species follow slightly different trends in agreement with literature (Parisi *et al* 2017, Olko and Bilski 2021). This could explain why the low-LET ^{4}He-ion measurement appears as an outlier when fitted against the current model, including data from all species. Noteworthy in this regard is that the measured detector efficiencies for that specific data point are inconsistent between the Al_2O_3:C,Mg and Al_2O_3:C films. As the films were irradiated together, this could point to an error in the handling of this sample.

The energy spectrum of the high-LET proton measurements is wide and with a somewhat mixed particle spectrum, making the presented calibrations applicable for treatments consisting of, e.g. spread out Bragg peaks (SOBPs) of protons. However, to conduct measurements in ^{4}He and ^{12}C SOBPs, it is necessary to extend the $\overline{\mathrm{LET}}_{\mathrm{D}}$ calibration curves with more high-LET data points, particularly for mixed particle fields.

Future investigations will address calibration for individual particle types, extension of the $\overline{\mathrm{LET}}_{\mathrm{D}}$ range covered by heavier ions, and assessment of the advantages of calibration against other RQMs.

$\overline{\mathrm{LET}}_{\mathrm{D}}$ assessment. As a demonstration of the system capabilities, we were able to retrieve the dose and $\overline{\mathrm{LET}}_{\mathrm{D}}$ map of a mono-energetic proton field delivered through a PMMA wedge to an Al_2O_3:C,Mg film as seen in figure 9. The developed system is capable of measuring dose and $\overline{\mathrm{LET}}_{\mathrm{D}}$ maps simultaneously with a spatial resolution of 1.0 mm^2 from detectors just 125 μm thick of sizes up to (190×190) mm^2. Validation of the system capabilities against independent treatment facilities will be the scope of future investigations.

To our knowledge, this is the first time that simultaneous dose and $\overline{\mathrm{LET}}_{\mathrm{D}}$ maps have been reported from such a large detector area without *a priori* information. Systems worth mentioning in this regard include the RPL-based system developed by Saint-Hubert *et al* (2021), which was demonstrated to derive LET maps from Al_2O_3:C,Mg films using a laser-scanning readout with a spot size of 1.6 mm. Other approaches have been demonstrated by Gajewski *et al* (2016) and Sadel *et al* (2023), using TL- and OSL-based detectors, respectively, relying on imaging-based readout systems, which are capable of providing sub-mm spatial resolutions. Especially popular for 2D dose measurements are the use of radiochromic films (Battum *et al* 2008, Kawashima *et al* 2020, An *et al* 2022), relying on flat-bed scanners for readout, which can provide sub-mm pixel resolutions with acceptable signal-to-noise ratios (Khan *et al* 2024). Common for all these systems is that they rely on *a priori* information and/or multiple irradiations and/or multiple detectors to determine $\overline{\mathrm{LET}}_{\mathrm{D}}$, and they require up to several system-specific correction factors to be applied to the readout.

The system presented in this work provides simultaneous measurements in 2D of auto-corrected dose and $\overline{\mathrm{LET}}_{\mathrm{D}}$ from a single irradiation, using a single detector, without prior information. With these properties, it provides a promising expansion of studies relying on, e.g. anthroponomorphic phantoms (Stengl *et al* 2023, Bobić *et al* 2024) to include 2D dose and $\overline{\mathrm{LET}}_{\mathrm{D}}$ mapping of large areas, thereby paving the way for experimental validation of treatment plans in ion-beam therapy.

5. Conclusion

We have developed and demonstrated a novel optical readout system capable of simultaneously measuring 2D dose and $\overline{\mathrm{LET}}_{\mathrm{D}}$ maps from differently doped Al_2O_3 films measuring up to $(190 \times 190)\,\mathrm{mm}^2$ with a spatial resolution of $(1.0 \times 1.0)\,\mathrm{mm}^2$. The system was calibrated using irradiations with ^{1}H-, ^{4}He-, and ^{12}C-ions, and its performance was demonstrated by mapping a proton Bragg curve in 2D. The system exhibits MDDs below 25 mGy and provides $\overline{\mathrm{LET}}_{\mathrm{D}}$ measurements without requiring prior knowledge of the dose. To our knowledge, this is the first passive detector system capable of measuring dose and $\overline{\mathrm{LET}}_{\mathrm{D}}$ simultaneously over large areas with high spatial resolution with no need for *a priori* information. In light of the results presented in this work, we envision that the developed system could be applied for experimental quality assurance of LET-optimized treatment plans in ion-beam therapy and assessment of the radiobiological effectiveness.

Data availability statement

The data that support the findings of this study are openly available at the following URL/DOI: https://doi.org/10.5281/zenodo.15308420.

Acknowledgments

Silvia Fabiano and Riccardo Dal Bello from the Department of Radiation Oncology, University Hospital Zurich, Zurich, Switzerland, are acknowledged for their help with homogenous photon irradiations, which were highly valued during the initial characterization stages. This work was funded by the Swiss National Science Foundation (SNSF) under the SPARK Grant Number CRSK-2_220796/1.

ORCID iDs

Mads Lykke Jensen 0000-0001-9534-9034
Michele Togno 0000-0001-6840-814X
Iván D Muñoz 0000-0001-5183-3705
Stephan Brons 0000-0002-4695-0816
Oliver Jäkel 0000-0002-6056-9747
Eduardo G Yukihara 0000-0002-4615-6698
Jeppe Brage Christensen 0000-0002-6894-381X

References

Agosteo S, Cirrone G A, Colautti P, Cuttone G, D'Angelo G, Fazzi A, Introini M V, Moro D, Pola A and Varoli V 2010 Study of a silicon telescope for solid state microdosimetry: preliminary measurements at the therapeutic proton beam line of catana *Radiat. Meas.* **45** 1284–9

Ahmed M F, Schnell E, Ahmad S and Yukihara E G 2016a Image reconstruction algorithm for optically stimulated luminescence 2D dosimetry using laser-scanned Al_2O_3:C and Al_2O_3:C,Mg films *Phys. Med. Biol.* **61** 7484

Ahmed M F, Shrestha N, Schnell E, Ahmad S, Akselrod M S and Yukihara E G 2016b Characterization of Al_2O_3 optically stimulated luminescence films for 2D dosimetry using a 6 MV photon beam *Phys. Med. Biol.* **61** 7551
An S, il Pak S, Jeong S, Min S, Kim T J, Shin D, Lim Y, Jeong J H, Kim H and Lee S B 2022 Measurement of proton beam dose-averaged linear energy transfer using a radiochromic film *Prog. Med. Phys.* **33** 80–87
Bachiller-Perea D, Zhang M, Fleta C, Quirion D, Bassignana D, Gómez F and Guardiola C 2022 Microdosimetry performance of the first multi-arrays of 3D-cylindrical microdetectors *Sci. Rep.* **12** 1–15
Battum L J V, Hoffmans D, Piersma H and Heukelom S 2008 Accurate dosimetry with gafchromic^{TM} EBT film of a 6 MV photon beam in water: what level is achievable? *Med. Phys.* **35** 704–16
Benton E R and Benton E V 2001 Space radiation dosimetry in low-earth orbit and beyond *Nucl. Instrum. Methods Phys. Res. B* **184** 255–94
Bianchi A, Selva A, Pasquato F, Rossignoli M, Minarello A, Fazzi A and Conte V 2024 Microdosimetric measurements for LET monitoring in proton therapy. The development of engineered mini-TEPCs for clinical applications: first results *Radiat. Meas.* **177** 107271
Bilski P 2006 Dosimetry of densely ionising radiation with three LiF phosphors for space applications *Radiat. Prot. Dosim.* **120** 397–400
Birks J B 1951 Scintillations from organic crystals: specific fluorescence and relative response to different radiations *Proc. Phys. Soc. A* **64** 874
Bobić M *et al* 2024 Optically stimulated luminescence dosimeters for simultaneous measurement of point dose and dose-weighted LET in an adaptive proton therapy workflow *Front. Oncol.* **13** 1333039
Bolzonella M *et al* 2022 Neutron personal dosimetry using polyallyl diglycol carbonate (PADC): current status, best practices and proposed research *Phys. Open* **12** 100114
Bossin L, Jensen M L, King G E and Yukihara E G 2025 Towards a fully automated instrument for the advanced characterisation of trapped-charge luminescence signals: the nautilus proof-of-concept *Radiat. Meas.* submitted
Bøtter-Jensen L, Larsen N A, Markey B G and McKeever S W 1997 Al_2O_3:C as a sensitive OSL dosemeter for rapid assessment of environmental photon dose rates *Radiat. Meas.* **27** 295–8
Christensen J B *et al* 2024b Status of LET assessment with active and passive detectors in ion beams *Radiat. Meas.* **177** 107252
Christensen J B, Bossin L, Muñoz I D, Stengl C, Vedelago J and Yukihara E G 2024a Optically stimulated luminescence detectors for LET determination and dosimetry in ion beam therapy *Radiat. Meas.* **177** 107270
Christensen J B, Muñoz I D, Bassler N, Stengl C, Bossin L, Togno M, Safai S, Jäkel O and Yukihara E G 2023 Optically stimulated luminescence detectors for dosimetry and LET measurements in light ion beams *Phys. Med. Biol.* **68** 155001
Christensen J B, Togno M, Bossin L, Pakari O V, Safai S and Yukihara E G 2022 Improved simultaneous LET and dose measurements in proton therapy *Sci. Rep.* **12** 1–10
Conte V *et al* 2020 Microdosimetry of a therapeutic proton beam with a mini-TEPC and a microplus-bridge detector for RBE assessment *Phys. Med. Biol.* **65** 245018
Cortés-Giraldo M A and Carabe A 2015 A critical study of different Monte Carlo scoring methods of dose average linear-energy-transfer maps calculated in voxelized geometries irradiated with clinical proton beams *Phys. Med. Biol.* **60** 2645
Deng W, Yang Y, Liu C, Bues M, Mohan R, Wong W W, Foote R H, Patel S H and Liu W 2021 A critical review of LET-based intensity-modulated proton therapy plan evaluation and optimization for head and neck cancer management *Int. J. Part. Ther.* **8** 36–49
Faddegon B, Ramos-Méndez J, Schuemann J, McNamara A, Shin J, Perl J and Paganetti H 2020 The topas tool for particle simulation, a Monte Carlo simulation tool for physics, biology and clinical research *Phys. Medica* **72** 114–21
Félix-Bautista R, Hamad Y, Yáñez-González T, Ochoa-Parra P, Granja C, Martišíková M, Mairani A and Gehrke T 2024 Towards precise LET measurements based on energy deposition of therapeutic ions in Timepix3 detectors *Phys. Med. Biol.* **69** 125030
Gajewski J, Kłosowski M and Olko P 2016 Two-dimensional thermoluminescence dosimetry system for proton beam quality assurance *Radiat. Meas.* **90** 224–7
Garbacz M *et al* 2021 Study of relationship between dose, LET and the risk of brain necrosis after proton therapy for skull base tumors *Radiother. Oncol.* **163** 143–9
Guan F *et al* 2018 RBE model-based biological dose optimization for proton radiobiology studies *Int. J. Part. Ther.* **5** 160–71
Guardiola C, Bachiller-Perea D, Kole E M, Fleta C, Quirion D, Marzi L D and Gómez F 2023 First experimental measurements of 2D microdosimetry maps in proton therapy *Med. Phys.* **50** 570–81
Hahn C *et al* 2022 Towards harmonizing clinical linear energy transfer (LET) reporting in proton radiotherapy: a European multi-centric study *Acta Oncol.* **61** 206–14
IAEA-TRS-398 2024 *Techincal Reports Sereis No.* 398 (International Atomic Energy Agency) (https://doi.org/10.61092/iaea.ve7q-y94k)
ICRU-85 2011 ICRU report No. 85: fundamental quantities and units for ionizing radiation *J. ICRU* **11** 5–6
ISO-11929-1 2019 International Standard 11929-1 *Technical Report* (International Organization for Standardization)
Janson M, Glimelius L, Fredriksson A, Traneus E and Engwall E 2024 Treatment planning of scanned proton beams in raystation *Med. Dosimetry* **49** 2–12
Kalholm F, Grzanka L, Toma-Dasu I and Bassler N 2023 Modeling RBE with other quantities than LET significantly improves prediction of in vitro cell survival for proton therapy *Med. Phys.* **50** 651–9
Kalholm F, Grzanka L, Traneus E and Bassler N 2021 A systematic review on the usage of averaged LET in radiation biology for particle therapy *Radiother. Oncol.* **161** 211–21
Kalholm F, Toma-Dasu I, Traneus E and Bassler N 2024 Novel radiation quality metrics accounting for proton energy spectra for RBE proton models *Med. Phys.* **51** 5773–82
Karger C P, Glowa C, Peschke P and Kraft-Weyrather W 2021 The RBE in ion beam radiotherapy: *in vivo* studies and clinical application *Z. Med. Phys.* **31** 105–21
Kawashima M, Matsumura A, Souda H and Tashiro M 2020 Simultaneous determination of the dose and linear energy transfer (LET) of carbon-ion beams using radiochromic films *Phys. Med. Biol.* **65** 125002
Khan R, Rahimi R, Fan J and Chen K L 2024 Systematic characterization of new EBT4 radiochromic films in clinical x-ray beams *Biomed. Phys. Eng. Express* **11** 015006
Khan R, Rahimi R, Fan J, Zhao L and Das I J 2010 Gafchromic EBT film dosimetry in proton beams *Phys. Med. Biol.* **55** N291
Klimpki G, Mescher H, Akselrod M S, Jakel O and Greilich S 2016 Fluence-based dosimetry of proton and heavier ion beams using single track detectors *Phys. Med. Biol.* **61** 1021
Lechner W and Palmans H 2025 Uncertainty estimation for dosimetry in radiation oncology *Phys. Imaging Radiat. Oncol.* **34** 100773

Lühr A, von Neubeck C, Helmbrecht S, Baumann M, Enghardt W and Krause M 2017 Modeling *in vivo* relative biological effectiveness in particle therapy for clinically relevant endpoints *Acta Oncol.* **56** 1392–8
McIntyre M, Wilson P, Gorayski P and Bezak E 2023 A systematic review of LET-guided treatment plan optimisation in proton therapy: identifying the current state and future needs *Cancers* **15** 4268
Miyamoto Y, Nanto H, Kurobori T, Fujimoto Y, Yanagida T, Ueda J, Tanabe S and Yamamoto T 2014 RPL in alpha particle irradiated Ag^{+}-doped phosphate glass *Radiat. Meas.* **71** 529–32
Mohan R 2022 A review of proton therapy—current status and future directions *Precis. Radiat. Oncol.* **6** 164–76
Muñoz I D *et al* 2024 Linear energy transfer measurements and estimation of relative biological effectiveness in proton and helium ion beams using fluorescent nuclear track detectors *Int. J. Radiat. Oncol. Biol. Phys.* **120** 205–15
Nascimento L F, Leblans P, van der Heyden B, Akselrod M, Goossens J, Verellen D and Kodaira S 2022 Characterization and quenching correction for a 2D real time radioluminescent system in therapeutic proton and carbon charged beams *Sens. Actuators A* **345** 113781
Niemierko A, Schuemann J, Niyazi M, Giantsoudi D, Maquilan G, Shih H A and Paganetti H 2021 Brain necrosis in adult patients after proton therapy: is there evidence for dependency on linear energy transfer? *Int. J. Radiat. Oncol. Biol. Phys.* **109** 109–19
Olko P and Bilski P 2021 Microdosimetric understanding of dose response and relative efficiency of thermoluminescence detectors *Radiat. Prot. Dosim.* **192** 165–77
Paganetti H *et al* 2019 Report of the AAPM TG-256 on the relative biological effectiveness of proton beams in radiation therapy *Med. Phys.* **46** e53–e78
Parisi A, Furutani K M, Sato T and Beltran C J 2024 LET-based approximation of the microdosimetric kinetic model for proton radiotherapy *Med. Phys.* **51** 7589–605
Parisi A, Olko P, Swakoń J, Horwacik T, Jabłoński H, Malinowski L, Nowak T, Struelens L and Vanhavere F 2020 Modeling the radiation-induced cell death in a therapeutic proton beam using thermoluminescent detectors and radiation transport simulations *Phys. Med. Biol.* **65** 015008
Parisi A, Van Hoey O, Mégret P and Vanhavere F 2017 The influence of the dose assessment method on the LET dependence of the relative luminescence efficiency of LiF:Mg,Ti and LiF:Mg,Cu,P *Radiat. Meas.* **98** 34–40
Payne S A, Moses W W, Sheets S, Ahle L, Cherepy N J, Sturm B, Dazeley S, Bizarri G and Choong W S 2011 Nonproportionality of scintillator detectors: theory and experiment. II *IEEE Trans. Nucl. Sci.* **58** 3392–402
Perl J, Shin J, Schümann J, Faddegon B and Paganetti H 2012 TOPAS: an innovative proton Monte Carlo platform for research and clinical applications *Med. Phys.* **39** 6818–37
Poikela T *et al* 2014 Timepix3: a 65K channel hybrid pixel readout chip with simultaneous ToA/ToT and sparse readout *J. Instrum.* **9** C05013
Sadel M, Grzanka L, Swakon J, Baran J, Gajewski J and Bilski P 2023 Optically stimulated luminescent response of the limgpo4 silicone foils to protons and its dependence on proton energy *Materials* **16** 1978
Saint-Hubert M D, Castellano F, Leblans P, Sterckx P, Kodaira S, Swakoń J and de Freitas Nascimento L 2021 Characterization of 2D Al_2O_3:C,Mg radiophotoluminescence films in charged particle beams *Radiat. Meas.* **141** 106518
Saint-Hubert M D, de Souza L F, Kodaira S, Swakoń J and de Freitas Nascimento L 2019 Luminescence efficiency of Al_2O_3:C,Mg radiophotoluminescence in charged particle beams *Radiat. Meas.* **123** 54–57
Samnøy A T, Ytre-Hauge K S, Malinen E, Tran L, Rosenfeld A, Povoli M, Kok A, Summanwar A and Röhrich D 2020 Microdosimetry with a 3D silicon on insulator (SOI) detector in a low energy proton beamline *Radiat. Phys. Chem.* **176** 109078
Scholz M, Friedrich T, Magrin G, Colautti P, Ristić-Fira A and Petrović I 2020 Characterizing radiation effectiveness in ion beam therapy part I: introduction and biophysical modeling of RBE using the lemiv *Front. Phys.* **8** 548651
Sechopoulos I, Rogers D W, Bazalova-Carter M, Bolch W E, Heath E C, McNitt-Gray M F, Sempau J and Williamson J F 2018 RECORDS: improved Reporting of montE CarlO RaDiation transport Studies: report of the AAPM Research Committee Task Group 268 *Med. Phys.* **45** e1–e5
Sholom S and McKeever S W 2023 Silver molecular clusters and the properties of radiophotoluminescence of alkali-phosphate glasses at high dose *Radiat. Meas.* **163** 106924
Somogyi G, Grabisch K, Scherzer R and Enge W 1976 Revision of the concept of registration threshold in plastic track detectors *Nucl. Instrum. Methods* **134** 129–41
Sørensen B S, Overgaard J and and N B 2011 In vitro RBE-LET dependence for multiple particle types *Acta Oncol.* **50** 757–62
Stengl C *et al* 2023 A phantom to simulate organ motion and its effect on dose distribution in carbon ion therapy for pancreatic cancer *Phys. Med. Biol.* **68** 245013
Tran L T *et al* 2021 Silicon 3D microdosimeters for advanced quality assurance in particle therapy *Appl. Sci.* **12** 328
Traneus E and Ödén J 2019 Introducing proton track-end objectives in intensity modulated proton therapy optimization to reduce linear energy transfer and relative biological effectiveness in critical structures *Int. J. Radiat. Oncol. Biol. Phys.* **103** 747–57
Underwood T S and McMahon S J 2019 Proton relative biological effectiveness (RBE): a multiscale problem *Br. J. Radiol.* **92** 20180004
Vestergaard A, Kallehauge J F, Muhic A, Carlsen J F, Dahlrot R H, Lukacova S, Haslund C A, Lassen-Ramshad Y, Worawongsakul R and Høyer M 2025 Mixed effect model confirms increased risk of image changes with increasing linear energy transfer in proton therapy of gliomas *Radiother. Oncol.* **204** 110716
Yukihara E G, Doull B A, Ahmed M, Brons S, Tessonnier T, Jäkel O and Greilich S 2015 Time-resolved optically stimulated luminescence of Al_2O_3:C for ion beam therapy dosimetry *Phys. Med. Biol.* **60** 6613–38
Yukihara E G and McKeever S W S 2006 Spectroscopy and optically stimulated luminescence of Al_2O_3:C using time-resolved measurements *J. Appl. Phys.* **100** 083512
Yukihara E G and McKeever S W S 2011 *Optically Stimulated Luminescence: Fundamentals and Applications* 1st edn (Wiley) (https://doi.org/10.1002/9780470977064)
Yukihara E G, McKeever S W, Andersen C E, Bos A J, Bailiff I K, Yoshimura E M, Sawakuchi G O, Bossin L and Christensen J B 2022 Luminescence dosimetry *Nat. Rev. Methods Primers* **2** 1–21